ENGINEERING

Kirigami enabled reconfigurable three-dimensional evaporator arrays for dynamic solar tracking and high efficiency desalination

Hao Li[1]†, Weixin Zhang[1,2]†, Xi Liao[3,4]*, Lizhi Xu[1,2,5]*

A kirigami-engineered composite hydrogel membrane is exploited for the construction of three dimensional (3D) solar-tracking evaporator arrays with outstanding evaporation performance and salt tolerance. The hybrid nanofiber network in the hydrogel membrane offers favorable water transport dynamics combined with excellent structural robustness, which are beneficial for the engineering of 3D dynamic structures. Periodic triangular cuts patterned into the membrane allow formation and reconfiguration of 3D conical arrays controlled by uniaxial stretching. With these structures, the tilt angles of the membrane surface are actively tuned to follow the solar trajectory, leading to a solar evaporation rate ~80% higher than that of static planar devices. Furthermore, the tapered 3D flaps and their micro-structured surfaces are capable of localized salt crystallization for prolonged solar desalination, enabling a stable evaporation rate of 3.4 kg m^{-2} $hour^{-1}$ even in saturated brine. This versatile design may facilitate the implementation of solar evaporators for desalination and provide inspirations for other soft functional devices with dynamic 3D configurations.

INTRODUCTION

Desalination via interfacial solar evaporators (ISEs) is regarded as a cost-effective and carbon-zero approach to addressing the worldwide clean water shortage (*1*, *2*). It also features simple configuration facilitating the development of portable systems. However, most of the existing ISEs exhibit insufficient efficiency in energy harvesting and clean water production, which may limit their practical applications. Extensive research efforts were devoted to designing ISEs with enhanced efficiency, such as promoting water supply (*3*, *4*), minimizing heat loss (*5*, *6*), reducing vaporization enthalpy (*7*, *8*), capturing ambient energy (*9*, *10*), and other interfacial designs (*11*–*13*). ISEs with three-dimensional (3D) structures were also proposed, which present increased surface area for evaporation. They also facilitate localized salt crystallization, which is helpful for continuous freshwater generation from high-salinity brine (*14*–*17*). However, the performance enhancement of these for ISEs was usually demonstrated in an ideal laboratory setting with static illumination. Their fixed configurations can barely accommodate the dynamic solar trajectory, resulting in a compromised performance in real-world applications (*18*). Recent works explored the integration of ISEs with solar tracking platform commonly used in photovoltaics (*19*, *20*), but the associated increase of size and complexity of the system may hinder their scalable implementation.

Kirigami provides great inspirations for the design of reconfigurable devices with simple actuation mechanisms. With a pattern of cuts incorporated into a solid membrane, reversible transformation of 3D structures becomes possible with planar deformation applied at the periphery of the base membrane (*21*). Kirigami has enabled various reconfigurable devices for soft robots (*22*, *23*), wearable electronics (*24*, *25*), and energy harvesters (*26*), among others (*27*–*29*). Recently, kirigami/origami designs were exploited for the engineering of solar trackable photovoltaics (*30*–*34*), suggesting a route for designing ISEs with dynamic configurations. Nevertheless, the complex mass transfer processes involved in solar evaporation would require distinct considerations on structural design and materials configuration. A tradeoff may exist between intrinsic water evaporation characteristics of the materials and their mechanical properties for structural reconfiguration. For instance, hydrogels are good candidates for ISEs due to their water-rich microscopic networks and the reduced evaporation enthalpy. However, their low modulus and brittle nature create difficulties for kirigami cutting and deterministic formation of stable 3D structures.

We recently found that composite hydrogels involving aramid nanofibers (ANFs) are advantageous for the engineering of ISEs (*35*). Their tunable open porous networks enable an optimum combination of evaporation performance and salt tolerance. In addition, their high mechanical strength allows multiscale manufacturing of complex structures. Here, we use this materials platform and demonstrate kirigami-based hydrogel solar evaporators (KHSEs) tailored for dynamic solar tracking and high-efficiency desalination (Fig. 1A). In this scheme, periodic triangular cuts incorporated into the hydrogel membrane allow formation of a 3D conical array under simple tension (Fig. 1, C and D). These asymmetric 3D structures maximize air-liquid interfaces for evaporation and allow tuning of the surfaces to dynamically track the solar irradiation (Fig. 1B). Furthermore, the tapered flaps and hierarchical surface structures of the hydrogel membrane facilitate localized salt crystallization (Fig. 1E), which enables a stable evaporation rate as high as 3.4 kg m^{-2} $hour^{-1}$ even in saturated brine. As demonstrated in a field test, the water production rate from dynamic KHSEs is 18 and 82% higher as compared to that of static KHSEs and conventional flat evaporators, respectively. The excellent performance and underlying design principles of KHSEs may facilitate the development of advanced water technologies and other reconfigurable 3D devices.

[1]Department of Mechanical Engineering, The University of Hong Kong, Hong Kong SAR 999077, China. [2]Advanced Biomedical Instrumentation Centre Limited, Hong Kong SAR 999077, China. [3]School of Construction Engineering, Shenzhen Polytechnic University, Shenzhen 518055, China. [4]Department of Architecture, The University of Hong Kong, Hong Kong SAR 999077, China. [5]Materials Innovation Institute for Life Sciences and Energy (MILES), The University of Hong Kong Shenzhen Institute of Research and Innovation (HKU-SIRI), Shenzhen 518057, China.
*Corresponding author. Email: xiliao22@szpu.edu.cn (X.L.); xulizhi@hku.hk (L.X.)
†These authors contributed equally to this work.

RESULTS

KHSEs is based on hydrogel membranes involving ANF network and polyvinyl alcohol (PVA) prepared by solution processing (*36*). After coating with polypyrrole (PPy) for photothermal conversion (fig. S1), the resultant hydrogel membrane was laser engraved with periodic triangular notches to obtain KHSE (Fig. 2A and fig. S2). In the present design, the composite nanofiber hydrogel is advantageous for the engineering of kirigami devices due to its high mechanical properties. The pristine ANF-PVA-PPy hydrogel membrane exhibits a high stretchability of ~120%, strength of ~8 MPa, and modulus of ~10 MPa (Fig. 2B). A high fracture energy up to ~2900 J m^{-2} is achieved (Fig. 2C), which allows patterning of kirigami cuts without

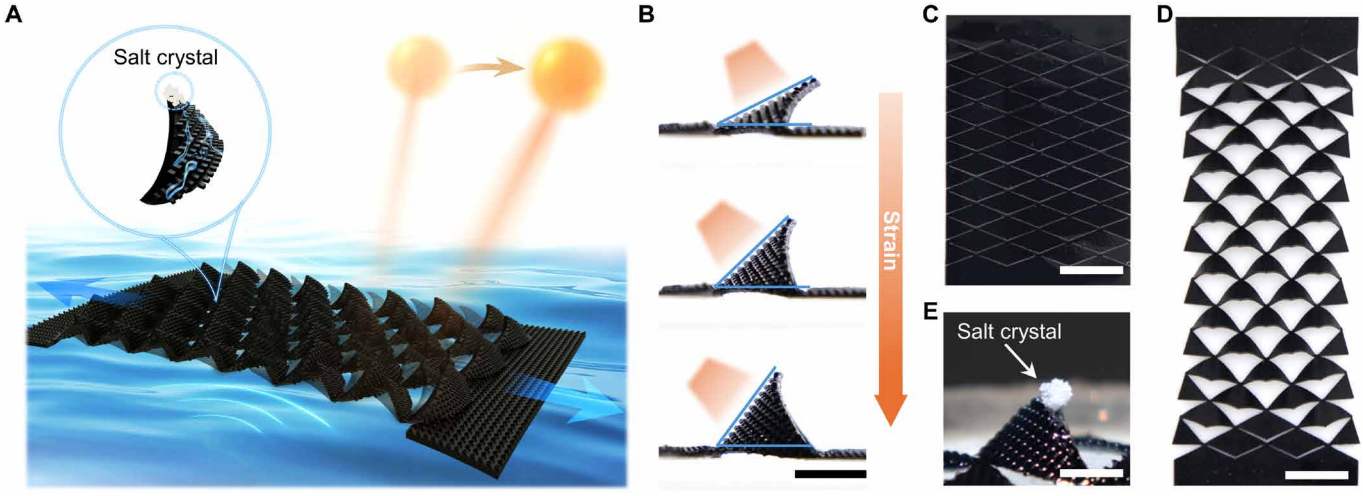

Fig. 1. Design of KHSEs. (**A**) Schematic of a large-scale KHSE with localized crystallization and dynamic solar tracking. (**B**) Solar tracking via coupling the tilt angle with incident sunlight by tuning the imposed strain. Scale bar, 1 cm. (**C** and **D**) A hydrogel membrane with periodic triangular notches (C) enables a 3D evaporator array under strain (D). Scale bars, 1 cm. (**E**) Localized crystallization by KHSE. Scale bar, 1 cm.

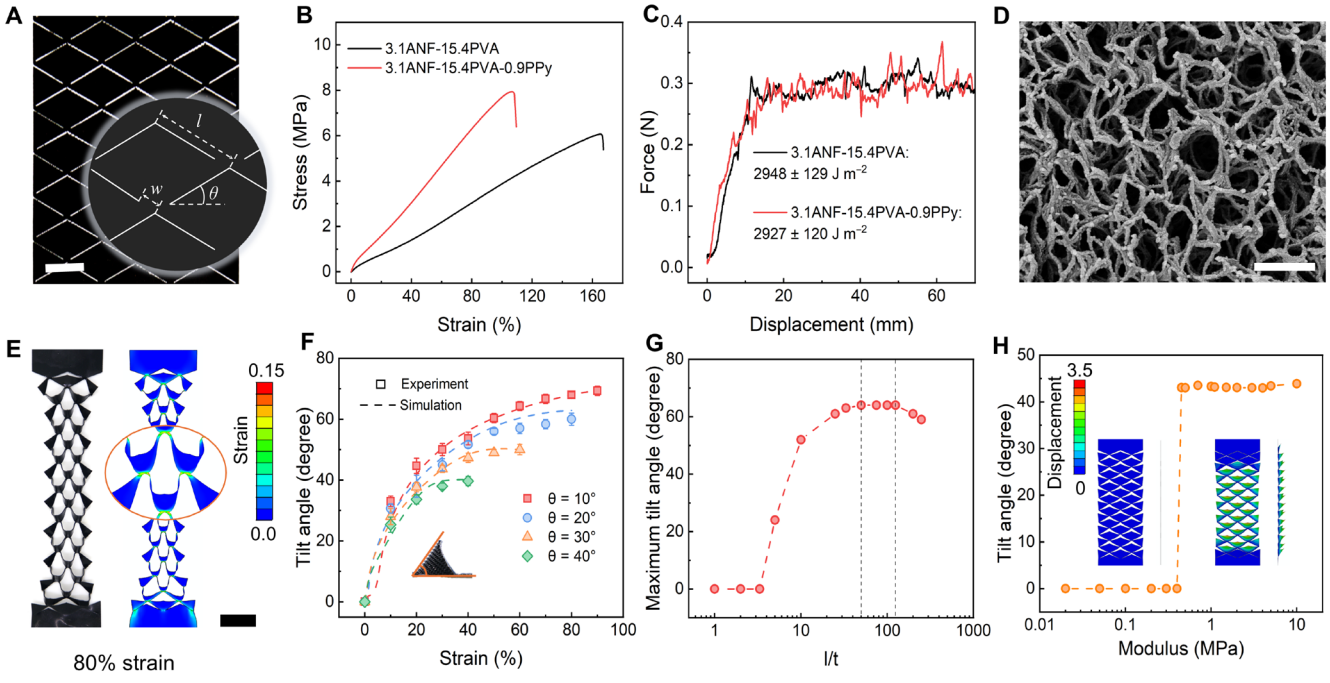

Fig. 2. Mechanical characterizations of KHSEs. (**A**) Schematic of the triangular cuts, including characteristic length (*l*), joint width (*w*), and angle (θ). The ratio between *l* and *w* is kept at 10:1. Scale bar, 1 cm. (**B**) Stress-strain curves of hydrogel membranes with and without PPy. (**C**) Fracture energy of hydrogel membranes with and without PPy evaluated by tearing tests. (**D**) Scanning electron microscopy (SEM) image of the hydrogel, showing an interconnected nanofiber network. Scale bar, 5 μm. (**E**) A stretched KHSE and strain distribution in the FEA-modeled membrane at 80% strain. Scale bar, 1 cm. (**F**) Tilt angle as a function of imposed strain for KHSEs with various θ. The inset indicates the definition of tilt angle. (**G**) Variation of maximum tilt angle of KHSEs with different *l*/*t*. The vertical dashed lines define an optimal range. (**H**) Variation of tilt angle in KHSEs with varying modulus at 20% strain. The inset demonstrates simulated out-of-plane deformation of samples with modulus of 0.4 MPa (left) and 1 MPa (right). The color label indicates the out-of-plane displacement.

crack propagation under stretching (*24*). Excellent mechanical properties of ANF-PVA hydrogel inherit from the interconnected ANF network toughened by PVA via extensive hydrogen bonds (Fig. 2D) (*36*). The loaded PPy is arranged along ANFs via π-π stacking and hydrogen bonding, providing efficient solar absorption without compromising the interconnected network and mechanical properties (*37*). This is difficult to achieve by other photothermal fillers such as carbon black nanoparticles and graphene oxide. For the kirigami structures, we used patterns of triangular cuts with variable characteristic length l, spacing w, and cut angle θ. These patterns allow asymmetric 3D deformation of KHSEs above water surface, leading to maximum interfaces for solar evaporation (Fig. 1A). A representative KHSE membrane ($l = 1$ cm, dimensionless ratio $l/w = 10$, and $\theta = 20°$) can withstand 80% of elongation without fracture (Fig. 2E). Finite element analysis (FEA) shows that the strain distributed in the elongated KHSE is well below the failure strain of the substrate, indicating its high structural robustness. The ANF-PVA-PPy membrane has a high fatigue threshold of ~147 J m^{-2}, allowing the cyclic operation of KHSE without crack extension (fig. S3).

We investigated 3D deformation patterns of KHSEs and their relationships with various design parameters, which provide essential information for the engineering of dynamic solar tracking functionality. Generally, uniaxial elongation of KHSEs involves three stages, including in-plane deformation (stage I, $\varepsilon < \varepsilon_{cri}$), post-buckling (stage II, $\varepsilon_{cri} < \varepsilon < \varepsilon_{bending}$), and bending-dominant deformation (stage III, $\varepsilon > \varepsilon_{bending}$) (note S1, fig. S8, and movie S1). Simulation results indicate that the structural design of KHSE has a considerable impact on the critical strain for buckling (ε_{cri}). Larger θ, l, and smaller t lead to an earlier onset of out-of-plane deformation induced by buckling (fig. S9). In the present design, both the stretchability and tilt angle (γ) are tunable by varying cut angles (Fig. 2F, figs. S4 to S6, and movie S2). The KHSE with 10° of cut angle exhibits a high stretchability of 200% and saturated tilt angle of 70° under 90% strain. The stretchability and maximum tilt angle both decrease with increasing cut angle, partly due to the increased structure stiffness (E_{K2}) at stage II. Higher E_{K2} of KHSE makes it easier to reach stage III, where deformation is primarily influenced by bending of kirigami units, and the tilt angle reaches saturation. This phenomenon was also observed in KHSEs with constant θ and various l and t, wherein lower E_{K2} is advantages for achieving larger elongation and maximum tilt angle (fig. S9).

The ratio of l/t also affects the range of tilt angle by influencing the stiffness (Fig. 2G and figs. S10 to S11). With the same l, the decreased thickness of the membrane results in a larger tilt angle, followed by a plateau that indicates the range for optimum design. The subsequent decline of maximum tilt angle might be ascribed to the decreased structural stiffness to a level that cannot resist the influence of gravity (fig. S9P). These results are applicable at various length scales (fig. S11B), providing universal guidelines for kirigami devices.

On the other hand, sufficient modulus of the hydrogel is necessary to resist the influence of gravity for the out-of-plane deformation. Soft hydrogels only undergo in-plane deformation under tension, without transitioning to stage II deformation throughout (fig. S13). From the perspective of bifurcation theory (*38*), the critical modulus could potentially serve as the bifurcation point for such a kirigami structure. The modulus of the hydrogel or the structural stiffness of the kirigami may be especially important to determine the post-buckling branches and the nonlinear dynamic behaviors. We developed a model with periodic boundary conditions to study the effect of gravity on the deformation of KHSE with different geometrical configurations and material properties (note S2). On the basis of analytical models and numerical simulations, we found that gravity plays an important role in choosing the post-buckling evolution pathway, in which substantial out-of-plane deformation occurs only when the modulus reaches a threshold value of 0.45 MPa (fig. S12). The results from theoretical modeling are consistent with the experimental observations (Fig. 2H, fig. S13, and movies S3 and S4). Therefore, the high modulus of ANF-PVA-PPy hydrogel is advantageous for KHSE as it can resist the influence of gravity and ensure robust pop-up 3D structures. After popping up, KHSEs with different moduli exhibit similar variation of tilt angle under strain (fig. S12A). This might be attributed to the increased structural stiffness of the curved flap, which ensures stable pop-up deformation far away from the bifurcation point. In addition, KHSE demonstrates stable deformation more than 1000 cycles of 80% elongation (fig. S14), indicating its durability for prolonged utilization.

Efficient water transport is vital for solar desalination in brine, especially for KHSE with a 3D evaporating interface rising above the water level. The solution-based processing of ANF-PVA-PPy enables generation of micropatterns via a simple molding method (fig. S2). Here, we patterned biomimetic 3D capillary ratchets on KHSE to facilitate the liquid suction (*39*). The antiswelling ANF-PVA-PPy hydrogel maintains the microstructure in the fully hydrated state (Fig. 3B). Scanning electron microscopy (SEM) images show the periodic arrangement of micro-ratchets on the surface, with the same width, height, and pitch of 250 μm and an inclination angle of 45° (Fig. 3C and fig. S15A). These micropatterns enable water to fully spread on a hydrogel strip (0.5 cm by 7 cm) in 0.3 s (Fig. 3D and movie S5), showing a greater water transfer capacity than that of smooth hydrogel (fig. S15B). Control experiments showed that ratchets with smaller width and pitch, as well as larger height, may be more effective for water spreading (fig. S15, C to E). An inclination angle of 45° is close to the optimum design for the ratchet (fig. S15F). For a stretched KHSE, localized salt crystallization during solar desalination in saturated brine is observed, which is related to the surface-enhanced water transfer and the 3D structure with tapered tip (Fig. 3E). The conical structure of the evaporator enables more efficient steam exclusion at the tip, which prevents steam accumulation around the evaporator and facilitates continuous evaporation, resulting in a more efficient evaporation at the tip (*15*, *18*). The variation of the evaporation rate can be validated by the decreasing surface temperature from the bottom to the top on KHSE (Fig. 3F and fig. S16). With the same energy input to the evaporator, the area with higher evaporation rate will consume more energy, leading to a lower temperature. As the most efficient evaporation is at the tip, the liquid here is easier to reach the critical concentration for crystallization, resulting in the tip-preferential crystallization. A KHSE involving an array of conical structures demonstrates consistent capability of localized crystallization when purifying saturated brine (Fig. 3, G and H and fig. S17). Furthermore, the reconfigurability of KHSE enables the removal of salt crystals from the evaporator by repeated stretch (fig. S18), providing an efficient approach to salt cleanup without manual intervention. Despite the successful solar desalination of saturated brine using KHSE, long-term reliability of this process could be further enhanced by integrating salt collection devices in future designs.

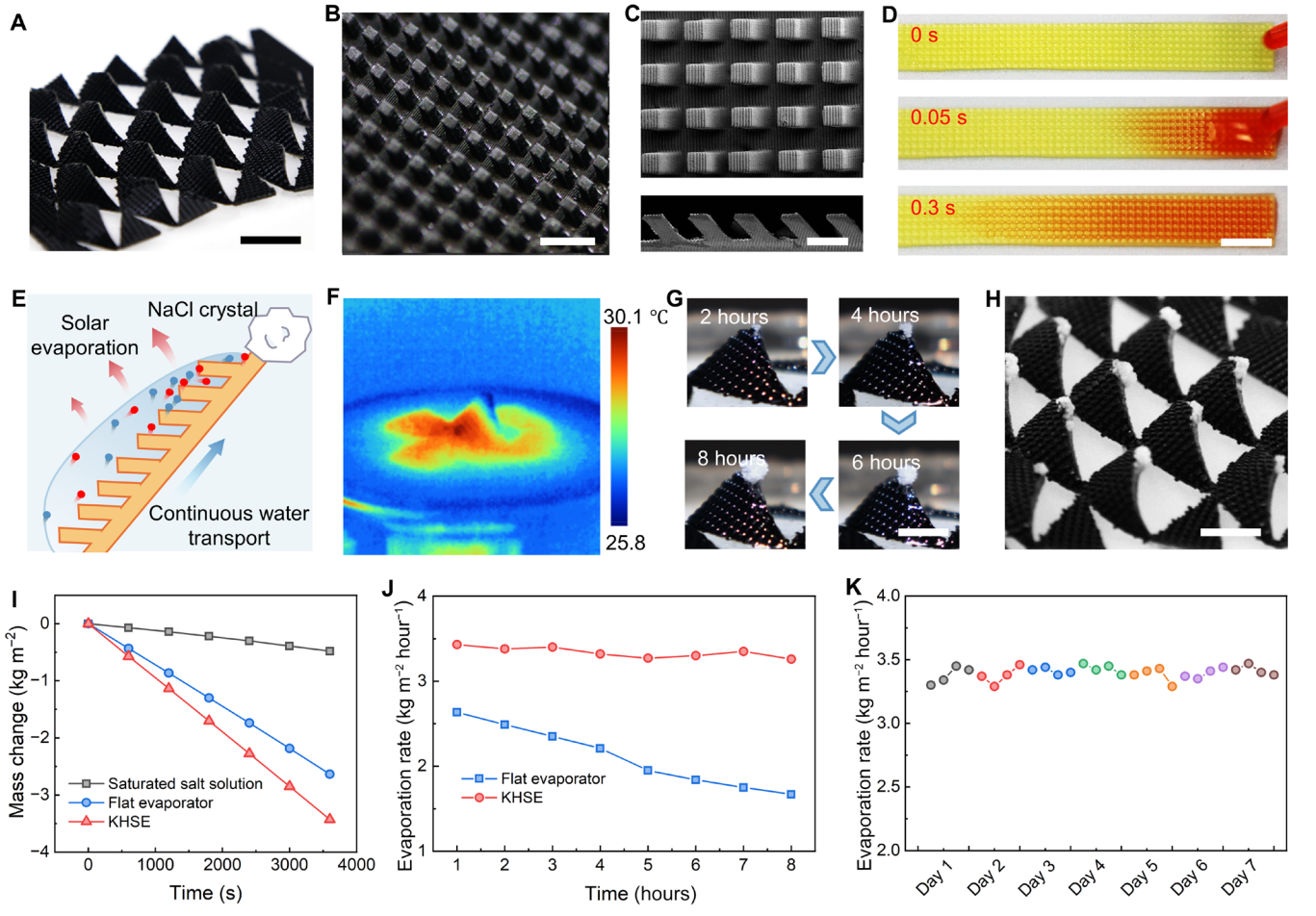

Fig. 3. Solar desalination performance of KHSEs. (**A**) Photograph of a KHSE with an array of 3D structures. Scale bar, 1 cm. (**B**) Optical image of micropatterns on KHSE at swollen state. Scale bar, 0.5 mm. (**C**) SEM images of top and side view of micropatterns. Scale bar, 500 μm. (**D**) Efficient water transfer on hydrogel membrane with micropatterns. Scale bar, 1 cm. (**E**) Schematic illustration indicating the mechanism of localized crystallization by KHSE. (**F**) Temperature distribution on KHSE under one sun illumination. (**G**) Sequential photographs displaying localized crystallization process of KHSE. Scale bar, 1 cm. (**H**) Photograph of localized salt crystallization on KHSE arrays. Scale bar, 1 cm. (**I**) Mass loss of saturated brine induced by KHSE under one sun illumination, with flat evaporator and pure saturated salt solution as controls. (**J**) Long-term evaporation test with saturated brine using KHSE and flat evaporator. (**K**) Stability of KHSE for treating saturated brine in 7 days. The evaporation lasts 8 hours per day.

A 3D KHSE with a tilt angle of 30° demonstrates a high evaporation rate of 3.4 kg m^{-2} $hour^{-1}$ under static illumination perpendicular to the water level, which is 1.3 and 7 times higher than that of flat evaporator and pure solution, respectively (Fig. 3I). Five factors may contribute to efficient evaporation. First, the evaporating interface is tilted away from the water surface, significantly reducing the heat loss to the bulk water, resulting in effective heat localization. Second, the out-of-plane deformation allows for additional evaporation at the backside, increasing the effective evaporative area. Third, the temperature gradient induces the Marangoni effect, driving the liquid from the high-temperature area to the low-temperature area under surface tension gradient (*15*). The high-temperature liquid is continuously transported to the top of the evaporator that shows the highest evaporation rate, realizing the reutilization of the thermal energy from the bottom. Redistribution of energy by liquid migration also improves the energy efficiency of KHSE. Fourth, the hydrated polymeric networks in KHSE reduce vaporization enthalpy by activating water molecules, which is validated by characterizing water states via Raman spectrum (fig. S19) (*7*). Last, the top of KHSE shows a surface temperature approximately 1.5°C lower than the ambient environment due to the evaporation cooling. Besides the solar input, the KHSE can capture extra energy from surroundings via thermal convection and radiation, which further enhances energy efficiency (*11*). In addition to the high evaporation rate, the KHSE also demonstrates more stable evaporation than that of flat evaporators in 8 hour of continuous evaporation (Fig. 3J and fig. S20). Stable evaporation of KHSE in saturated bine for 7 days (8 hours per day) indicates its durability for long-term solar desalination (Fig. 3K). In addition, the hydrogel membrane exhibits outstanding mechanical and chemical stability in strong brine under continuous solar irradiation over 2 weeks, ensuring the reliability of KHSE for prolonged utilization (fig. S21).

Generally, evaporation performance is evaluated in the laboratory with static and constant solar illumination, which is divergent from the real-world application (*18*). Actually, the deviation of the evaporator interface from the incident angle of sunlight causes

degraded evaporation performance (*30*). The ultimate evaporation value consists of two components, natural evaporation and solar-induced evaporation. The latter significantly decreases with the decline of the projected area and scales with the sine of solar altitude (fig. S22A). Assuming that solar is the sole energy source to the system, the evaporation rate (E_{evp}) can be described as the following equation

$$E_{evp} = E_n + \sin\alpha \cdot E_0 \quad (1)$$

where E_n, E_0, and α represent the natural evaporation, the solar-induced evaporation with vertically incident sunlight, and the solar altitude, respectively. This model is consistent with experimental observations (fig. S22B). The measured E_0 is 1.64 kg m^{-2} $hour^{-1}$, which accounts for 62% of the total evaporation, indicating the significance of stable projected area.

The reconfigurability of KHSE allows dynamic capturing of solar trajectory by aligning the tilt angle to the solar altitude (Fig. 4A). Analysis of projected area as a function of tilt angle and solar altitude provides quantitative guidance for the effective solar tracking (note S3)

$$A_p = A\sin(\alpha+\gamma)\left[1-\frac{\tan\gamma}{\tan(\alpha+\gamma)}\right](1+\varepsilon_T) \quad (2)$$

where A_p is the projected area, A is the initial area without deformation, α is the solar altitude, γ is the tilt angle, and ε_T is the transverse strain induced by Poisson's effect (Fig. 4B, figs. S23 to S26, and note S3). Insufficient tilt angle can lead to self-shadowing and misalignment between solar irradiation and evaporator, reducing the projected area. In the case of the solar altitude of 20°, a tilt angle of 70° is required. A decrease of 10° in the tilt angle will result in a reduction of more than 30% in the projected area due to the self-shadowing (fig. S26B). Therefore, the KHSE with the cut angle of 10° was used for solar tracking due to its large range of tilt angle and low transverse strain arising from low Poisson's ratio (fig. S23). With these characteristics, tracking sunlight with the solar altitude ranging from 20° to 90° becomes possible. This KHSE maintains 88% of projected area with the solar altitude of 20°, 158% higher than that of the flat evaporator (Fig. 4C). On the other hand, solar tracking at high solar altitude does not necessarily result in the maximum evaporation. When the solar altitude exceeds 60°, maximizing the projected area would lead to a very small tilt angle. However, the KHSE with low tilt angle may not fully exploit the advantages of 3D evaporation interfaces (Fig. 4D), resulting in a lower evaporation rate despite the large projected area. For an optimal configuration of KHSE, a static tilt angle of 30° is preferable as the solar altitude exceeds 60° (fig. S27).

For a KHSE with an array of 3D pop-up structures, the distribution of tilt angles among the structural units requires further attention. Units at the ends of the KHSE may exhibit lower tilt angle than those at the center of the array (fig. S28). We simulated a collection

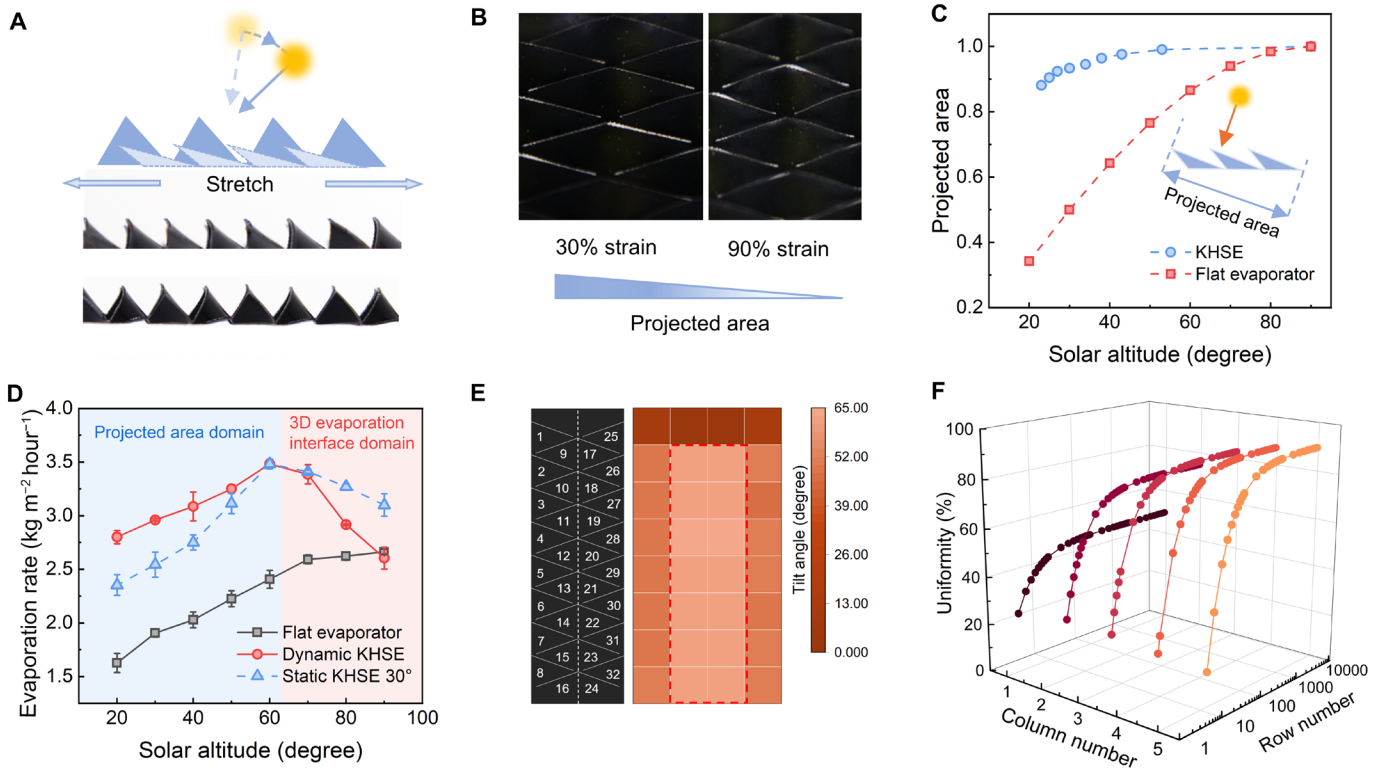

Fig. 4. Solar tracking performance of KHSEs. (**A**) Schematic of solar tracking with KHSE with imposed strain. (**B**) Photographs showing the projected area of a KHSE under different strains. The projected area decreases with the increase of imposed strain. (**C**) Comparison of projected area using KHSE and flat evaporator. (**D**) Evaporation performance of flat evaporator, dynamic KHSE for solar tracking, and static KHSE with a fixed tilt angle of 30°. (**E**) A color map showing the variation of tilt angles in a 1 × 8 KHSE under 60% strain. The area enclosed by dashed lines represents the uniform deformation region. (**F**) Uniformity of KHSE under strain as the function of column number and row number.

of KHSEs with different numbers of repeat units and investigated the distribution of tilt angles for each structural unit. By dividing each unit into four parts, the KHSE was gridded into $4N_cN_r$ regions, where N_r and N_c represent number of rows and number of columns, respectively (Fig. 4E, fig. S29, and note S4). Statistics of tilt angles in KHSEs were visualized as color maps to indicate the variation (Fig. 4E and fig. S30). The middle region of KHSE exhibits a uniform tilt angle distribution, with variations in angle less than 2°. The size of the uniform region changes with the size of the array. On the basis of the simulation results, we found an empirical relationship determining the size of the uniform region relative to the total area of the array (Fig. 4F and note S4)

$$P = \left[1 - \frac{7(2^{N_c-1} - 1) + N_r + 1}{2N_rN_c}\right] \times 100\% \quad (3)$$

This formula illustrates the impact of N_c and N_r on uniformity, facilitating the design of KHSEs with the desired deformation uniformity. For example, to achieve uniformity more than 80%, N_c and N_r should exceed 3 and 84, respectively (fig. S31).

Last, we evaluated the solar evaporation performance of KHSE in real-world conditions. The movement of the sun causes changes in both altitude and azimuth (Fig. 5A), representing variations in the angle of sunlight in vertical and horizontal directions, respectively. A prototype was developed to facilitate the angle coupling of KHSE with solar trajectory (Fig. 5B), which is driven by an algorithm for automatic solar tracking (note S5 and figs. S32 and S33). In this design, two steering engines (DSSERVO, DS3115) are integrated to control the stretch of KHSE and rotation of the evaporation system, respectively. We used a microcontroller (Arduino Uno) to program the rotation of the steering engines. Specifically, the solar altitude and azimuth were both calculated on the basis of the geographic position (22°16′50″N, 114°10′20″E, Hong Kong), date, and time (*40*). The coupled tilt angle and imposed strain to the KHSE were determined on the basis of the change of the solar altitude (figs. S27 and S34, D to F). A steering engine with pull rods was used to modulate the imposed strain on the KHSE by adjusting its rotation angle at different time intervals. The tracking of solar azimuth, on the other hand, was realized by the other steering engine integrated beneath the platform, programmed to rotate to specific angles over time. Notably, the solar tracking system was realized through preprogramed algorithms rather than solar detectors, which reduces the complexity of the system. The outdoor tests were conducted on sunny days from 8 a.m. to 4 p.m. with the automatic solar tracking system (Fig. 5C). In the meantime, changes in solar angles, solar intensity, temperature, and relative humidity were also recorded (Fig. 5, D and E, and fig. S34). An efficient water yield of 14.9 liter m^{-2} was achieved by KHSE with solar tracking, which is 18 and 85% higher than that of static KHSE (30° in tilt angle) and flat evaporator (0° in tilt angle) (Fig. 5F).

DISCUSSION

In summary, we have demonstrated a strategy for the construction of dynamic 3D evaporators with outstanding performance for solar desalination. The kirigami-structured composite hydrogel membranes enable deterministic assembly and reconfiguration of 3D structures for active solar tracking and efficient water transfer. This design fully leverages the dynamic reconfigurability of kirigami, achieving superior solar utilization compared to static 3D

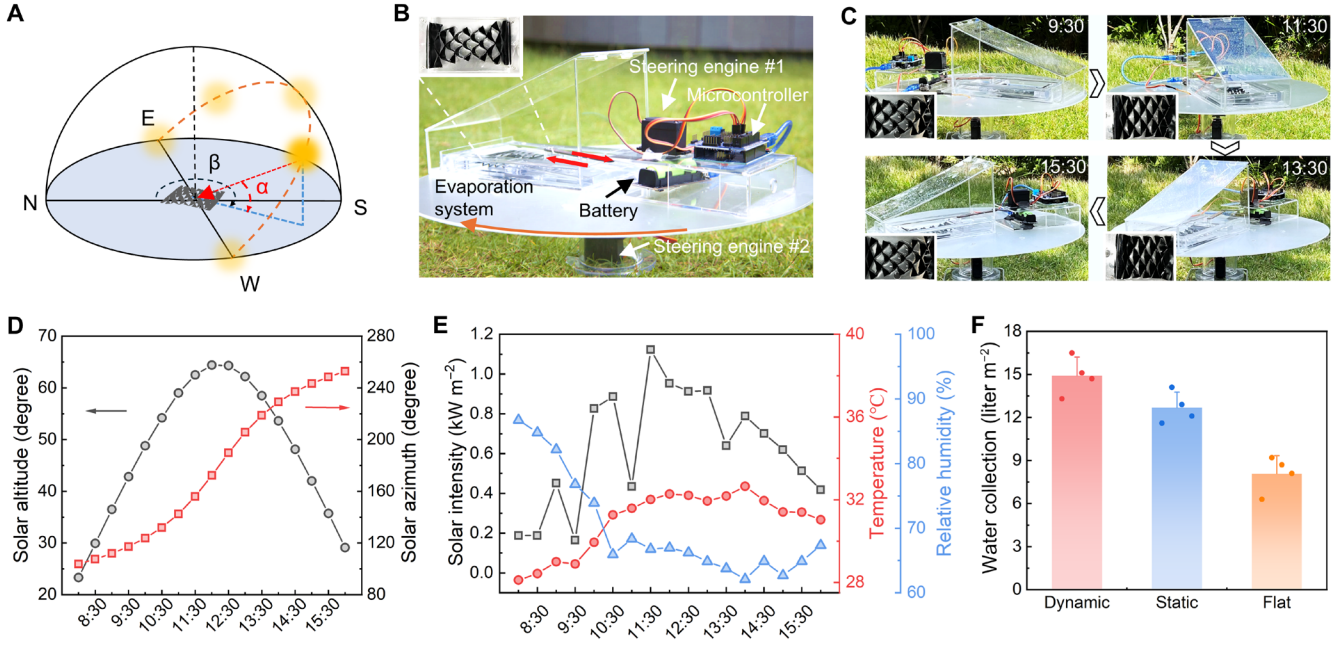

Fig. 5. Evaluation of KHSEs in field tests. (**A**) Schematic of solar trajectory. α and β are solar altitude and solar azimuth, respectively. (**B**) Photograph of the prototype including an evaporation system, a microcontroller, two steering engines, and a battery. Steering engine #1 and steering engine #2 are used for the cyclic stretching of KHSE and the rotation of the platform, respectively. The inset shows the KHSE. (**C**) Photographs displaying the solar tracking system from 8:00 to 16:00, with the insets indicating the configurations of the KHSE. (**D**) Variation of solar altitude and solar azimuth with time. (**E**) Changes of solar intensity, temperature, and humidity with time. (**F**) Water yield of dynamic KHSE, static KHSE with a fixed tilt angle of 30°, and flat evaporator.

evaporators (*16*, *18*, *41*). Systematic investigations of KHSE have revealed key relationships between base materials, structural designs, and 3D deformation behaviors of the membrane devices. These findings not only facilitate the development high-performance ISEs for practical applications but also provide insights for the engineering other kirigami devices for energy systems, flexible electronics, soft robots, etc. Nevertheless, scaling up the system for industrial applications would require further attention. For instance, tracking of the solar azimuth currently relies on the overall rotation of the solar desalination system. Simplifying the steering system with innovative designs would reduce the volume and cost. Further evaluation of environmental stability considering factors such as biodegradation or biological contamination would be important for determining the real lifespan of evaporators. Tuning the composition of hydrogels for extended functionality, such as heavy metal adsorption, would provide utility for the diverse needs in water treatment.

MATERIALS AND METHODS

Fabrication of KHSE

Preparation of ANF and PVA in dimethyl sulfoxide followed the methods reported elsewhere (*36*, *42*). Fabrication of ANF-PVA hydrogel membrane began with mixing 3 wt % ANF dispersion and 15 wt % PVA solution for a homogenous mixture. Then, ANF-PVA membrane was obtained by blade coating the mixture with controlled thickness, followed by solvent exchange with deionized water. The hydrogel membrane with micropatterns was produced by blade coating the mixture on a mold. Whereafter, the obtained hydrogel membrane was immersed into 0.1 M $FeCl_3$ solution and then exposed to pyrrole vapor to obtain ANF-PVA-PPy membrane. The periodic triangular notches were laser-patterned on the hydrogel membrane to obtain KHSE.

Structure characterization

The microstructures of KHSE were characterized using SEM (Hitachi S4800 FEG) after drying by critical point dryer (Tousimis Autosamdri 931). The solar absorption was obtained using ultraviolet-visible near infrared spectrometer (UV 3600I plus, Shimadzu). Raman spectra (Horiba Scientific LabRAM HR Evolution) were used to characterize water states in KHSE.

Mechanical tests

Mechanical performance of hydrogel membranes was evaluated on a tensile-compressive tester (Zwick Roell). The samples with the size of 30 mm by 5 mm by 0.22 mm were loaded with the stretching rate of 1% s^{-1}. Tearing test was carried out to evaluate the fracture energy (Γ) of hydrogel membranes (20 mm by 50 mm by 0.22 mm). Γ was calculated by $\Gamma = 2F/t$, where F and t represent steady-state tearing force and thickness of the membrane, respectively. For the fatigue test, a hydrogel sample (30 mm by 10 mm by 0.22 mm) was notched using a blade, followed by cyclic loaded with a fixed stretch. The hydrogel sample was sprayed with water regularly to prevent dehydration. The energy release rate (G) can be regulated by different stretch amplitudes (λ). G was calculated by $G = H \times W(\lambda)$, where H and $W(\lambda)$ represent the height of the sample and the elastic energy density, respectively. The crack advance (c) was recorded by a camera after 2000 cycles. Assuming that c increases linearly in cycle number (N), the crack advance per cycle was obtained by dc/dN.

Solar desalination performance of KHSE

Solar evaporation of KHSE was conducted under a solar simulator (Aulight, CEL-S500-T5) with the intensity of 1 kW m^{-2}. The incident solar angle was regulated by rotating the light outlet. The mass loss and temperature of KHSE was recorded using an electronic balance (Mettler Toledo) and an infrared camera (Fluke Ti480), respectively. The temperature and humidity during the evaporation tests were 25°C and 50%, respectively. Projected area of KHSE was estimated by capturing photos perpendicular to the tilt angle and measuring the area (fig. S24). For outdoor test, the solar intensity was measured using a solar power meter (Tenmars, TM-207). Ambient temperature and humidity were recorded using a multidetector (Renke, COS-03). The solar altitude and azimuth were collected from Hong Kong Observatory.

Numerical simulations

Numerical simulations were conducted with a commercial FEA package ABAQUS 2019 (SIMULIA). The Poisson's ratio was 0.27 for all simulations, which was obtained by experiment. Four-node shell elements (Abaqus element-type S4R with a mesh seed size of 0.1 mm) with reduced integration and hourglass control were used to discretize the KHSE with a mesh size much smaller than the length/width. Gravity was loaded on the whole model with an acceleration of 9.80 m/s^2, where the influence of gravity on post-buckling behaviors was concerned. The density of KHSEs was maintained as 1.03 g/cm^3. The tilt angle (γ) was calculated in a 3D rectangular coordinates system

$$\gamma = \tan^{-1}\left(\frac{z_1 - z_2}{y_1 - y_2}\right) \quad (4)$$

where (y_1, z_1) and (y_2, z_2) represent the coordinates of the vertex and the joint in a tilted flap, respectively. The deformation uniformity of KHSE was evaluated by statistically analyzing all tilt angles (Fig. 4, E and F, and figs. S29 to S31).

Supplementary Materials

This PDF file includes:

Supplementary Text
Figs. S1 to S34
Tables S1 and S2
Legends for movies S1 to S5
Legend for data S1
References

Other Supplementary Material for this manuscript includes the following:

Movies S1 to S5
Data S1

REFERENCES AND NOTES

1. P. Tao, G. Ni, C. Song, W. Shang, J. Wu, J. Zhu, G. Chen, T. Deng, Solar-driven interfacial evaporation. *Nat. Energy* **3**, 1031–1041 (2018).
2. Z. Wang, T. Horseman, A. P. Straub, N. Y. Yip, D. Li, M. Elimelech, S. Lin, Pathways and challenges for efficient solar-thermal desalination. *Sci. Adv.* **5**, eaax0763 (2019).
3. Z. Wang, X. Wu, F. He, S. Peng, Y. Li, Confinement capillarity of thin coating for boosting solar-driven water evaporation. *Adv. Funct. Mater.* **31**, 2011114 (2021).
4. H. Liang, Q. Liao, N. Chen, Y. Liang, G. Lv, P. Zhang, B. Lu, L. Qu, Thermal efficiency of solar steam generation approaching 100% through capillary water transport. *Angew. Chem. Int. Ed.* **58**, 19041–19046 (2019).
5. H. Ghasemi, G. Ni, A. M. Marconnet, J. Loomis, S. Yerci, N. Miljkovic, G. Chen, Solar steam generation by heat localization. *Nat. Commun.* **5**, 4449 (2014).
6. H. Liu, B. Chen, Y. Chen, M. Zhou, F. Tian, Y. Li, J. Jiang, W. Zhai, Bioinspired self-standing, self-floating 3d solar evaporators breaking the trade-off between salt cycle and heat localization for continuous seawater desalination. *Adv. Mater.* **35**, e2301596 (2023).

7. F. Zhao, X. Zhou, Y. Shi, X. Qian, M. Alexander, X. Zhao, S. Mendez, R. Yang, L. Qu, G. Yu, Highly efficient solar vapour generation via hierarchically nanostructured gels. *Nat. Nanotechnol.* **13**, 489–495 (2018).
8. X. Zhou, F. Zhao, Y. Guo, Y. Zhang, G. Yu, A hydrogel-based antifouling solar evaporator for highly efficient water desalination. *Energ. Environ. Sci.* **11**, 1985–1992 (2018).
9. X. Wu, Z. Wu, Y. Wang, T. Gao, Q. Li, H. Xu, All-cold evaporation under one sun with zero energy loss by using a heatsink inspired solar evaporator. *Adv. Sci.* **8**, 2002501 (2021).
10. X. Li, J. Li, J. Lu, N. Xu, C. Chen, X. Min, B. Zhu, H. Li, L. Zhou, S. Zhu, T. Zhang, J. Zhu, Enhancement of interfacial solar vapor generation by environmental energy. *Joule* **2**, 1331–1338 (2018).
11. Y. Shi, R. Li, Y. Jin, S. Zhuo, L. Shi, J. Chang, S. Hong, K.-C. Ng, P. Wang, A 3D photothermal structure toward improved energy efficiency in solar steam generation. *Joule* **2**, 1171–1186 (2018).
12. H. Zou, X. Meng, X. Zhao, J. Qiu, Hofmeister effect-enhanced hydration chemistry of hydrogel for high-efficiency solar-driven interfacial desalination. *Adv. Mater.* **35**, e2207262 (2023).
13. Y. Guo, X. Zhao, F. Zhao, Z. Jiao, X. Zhou, G. Yu, Tailoring surface wetting states for ultrafast solar-driven water evaporation. *Energ. Environ. Sci.* **13**, 2087–2095 (2020).
14. C. Chen, Y. Kuang, L. Hu, Challenges and opportunities for solar evaporation. *Joule* **3**, 683–718 (2019).
15. L. Wu, Z. Dong, Z. Cai, T. Ganapathy, N. X. Fang, C. Li, C. Yu, Y. Zhang, Y. Song, Highly efficient three-dimensional solar evaporator for high salinity desalination by localized crystallization. *Nat. Commun.* **11**, 521 (2020).
16. L. Li, N. He, B. Jiang, K. Yu, Q. Zhang, H. Zhang, D. Tang, Y. Song, Highly salt-resistant 3D hydrogel evaporator for continuous solar desalination via localized crystallization. *Adv. Funct. Mater.* **31**, 2104380 (2021).
17. Y. Xia, Q. Hou, H. Jubaer, Y. Li, Y. Kang, S. Yuan, H. Liu, M. W. Woo, L. Zhang, L. Gao, H. Wang, X. Zhang, Spatially isolating salt crystallisation from water evaporation for continuous solar steam generation and salt harvesting. *Energ. Environ. Sci.* **12**, 1840–1847 (2019).
18. H. Shan, Z. Ye, J. Yu, R. Wang, Z. Xu, Improving solar water harvesting via airflow restructuring using 3D vapor generator. *Device* **1**, 100065 (2023).
19. S. C. Singh, M. ElKabbash, Z. Li, X. Li, B. Regmi, M. Madsen, S. A. Jalil, Z. Zhan, J. Zhang, C. Guo, Solar-trackable super-wicking black metal panel for photothermal water sanitation. *Nat. Sustain.* **3**, 938–946 (2020).
20. Y. Bian, Z. Ye, G. Zhao, K. Tang, Y. Teng, S. Chen, L. Zhao, X. Yuan, S. Zhu, J. Ye, H. Lu, Y. Yang, L. Fu, S. Gu, Enhanced contactless salt-collecting solar desalination. *ACS Appl. Mater. Interfaces* **14**, 34151–34158 (2022).
21. L. Xu, T. C. Shyu, N. A. Kotov, Origami and kirigami nanocomposites. *ACS Nano* **11**, 7587–7599 (2017).
22. A. Rafsanjani, L. Jin, B. Deng, K. Bertoldi, Propagation of pop ups in kirigami shells. *Proc. Natl. Acad. Sci. U.S.A.* **116**, 8200–8205 (2019).
23. A. Rafsanjani, Y. Zhang, B. Liu, S. M. Rubinstein, K. Bertoldi, Kirigami skins make a simple soft actuator crawl. *Sci. Robot.* **3**, eaar7555 (2018).
24. H. Liu, H. Li, Z. Wang, X. Wei, H. Zhu, M. Sun, Y. Lin, L. Xu, Robust and multifunctional kirigami electronics with a tough and permeable aramid nanofiber framework. *Adv. Mater.* **34**, e2207350 (2022).
25. Z. Rao, Y. Lu, Z. Li, K. Sim, Z. Ma, J. Xiao, C. Yu, Curvy, shape-adaptive imagers based on printed optoelectronic pixels with a kirigami design. *Nat. Electron.* **4**, 513–521 (2021).
26. P.-K. Yang, Z.-H. Lin, K. C. Pradel, L. Lin, X. Li, X. Wen, J.-H. He, Z. L. Wang, Paper-based origami triboelectric nanogenerators and self-powered pressure sensors. *ACS Nano* **9**, 901–907 (2015).
27. S. Babaee, S. Pajovic, A. Rafsanjani, Y. Shi, K. Bertoldi, G. Traverso, Bioinspired kirigami metasurfaces as assistive shoe grips. *Nat. Biomed. Eng.* **4**, 778–786 (2020).
28. J. Li, R. Ran, H. Wang, Y. Wang, Y. Chen, S. Niu, P. E. Arratia, S. Yang, Aerodynamics-assisted, efficient and scalable kirigami fog collectors. *Nat. Commun.* **12**, 5484 (2021).
29. S. Xu, Z. Yan, K.-I. Jang, W. Huang, H. Fu, J. Kim, Z. Wei, M. Flavin, J. McCracken, R. Wang, A. Badea, Y. Liu, D. Xiao, G. Zhou, J. Lee, H. U. Chung, H. Cheng, W. Ren, A. Banks, X. Li, U. Paik, R. G. Nuzzo, Y. Huang, Y. Zhang, J. A. Rogers, Assembly of micro/nanomaterials into complex, three-dimensional architectures by compressive buckling. *Science* **347**, 154–159 (2015).
30. A. Lamoureux, K. Lee, M. Shlian, S. R. Forrest, M. Shtein, Dynamic kirigami structures for integrated solar tracking. *Nat. Commun.* **6**, 8092 (2015).
31. Y. Li, K. Chang, J. Chang, B. Yu, L. Liu, B. Liu, X. Zhao, W. Deng, Printed kirigami organic photovoltaics for efficient solar tracking. *Adv. Funct. Mater.* **32**, 2204004 (2022).
32. M. J. Yun, Y. H. Sim, D. Y. Lee, S. I. Cha, Automated shape-transformable self-solar-tracking tessellated crystalline Si solar cells using in-situ shape-memory-alloy actuation. *Sci. Rep.* **12**, 1597 (2022).
33. M. J. Yun, Y. H. Sim, D. Y. Lee, S. I. Cha, *Kirigami-inspired automatically self-inclining bifacial solar cell arrays to enhance energy yield under both sunny and cloudy conditions*, *iScience* **25**, 104649 (2022).
34. E. E. Evke, C. Huang, Y.-W. Wu, M. Arwashan, B. Lee, S. R. Forrest, M. Shtein, Kirigami-based compliant mechanism for multiaxis optical tracking and energy-harvesting applications. *Adv. Eng. Mater.* **23**, 2001079 (2021).
35. H. Li, W. Zhang, J. Liu, M. Sun, L. Wang, L. Xu, Self-assembled nanofibrous hydrogels with tunable porous network for highly efficient solar desalination in strong brine. *Adv. Funct. Mater.* **33**, 2308492 (2023).
36. L. Xu, X. Zhao, C. Xu, N. A. Kotov, Water-rich biomimetic composites with abiotic self-organizing nanofiber network. *Adv. Mater.* **30**, 1703343 (2018).
37. H. He, H. Li, A. Pu, W. Li, K. Ban, L. Xu, Hybrid assembly of polymeric nanofiber network for robust and electronically conductive hydrogels. *Nat. Commun.* **14**, 759 (2023).
38. N. Stoop, R. Lagrange, D. Terwagne, P. M. Reis, J. Dunkel, Curvature-induced symmetry breaking determines elastic surface patterns. *Nat. Mater.* **14**, 337–342 (2015).
39. S. Feng, P. Zhu, H. Zheng, H. Zhan, C. Chen, J. Li, L. Wang, X. Yao, Y. Liu, Z. Wang, Three-dimensional capillary ratchet-induced liquid directional steering. *Science* **373**, 1344–1348 (2021).
40. M. Cucumo, D. Kaliakatsos, V. Marinelli, General calculation methods for solar trajectories. *Renew. Energy* **11**, 223–234 (1997).
41. F. Ni, P. Xiao, C. Zhang, Y. Liang, J. Gu, L. Zhang, T. Chen, Micro–/macroscopically synergetic control of switchable 2D/3D photothermal water purification enabled by robust, portable, and cost-effective cellulose papers. *ACS Appl. Mater. Interfaces* **11**, 15498–15506 (2019).
42. J. Zhu, M. Yang, A. Emre, J. H. Bahng, L. Xu, J. Yeom, B. Yeom, Y. Kim, K. Johnson, P. Green, N. A. Kotov, Branched aramid nanofibers. *Angew. Chem. Int. Ed.* **56**, 11744–11748 (2017).
43. L. D. Landau, E. M. Lifshitz, A. d. M. Kosevich, L. P. Pitaevskii, *Theory of Elasticity* (Elsevier, 1986), vol. 7, 187 p.
44. S. P. Timoshenko, J. M. Gere, *Theory of Elastic Stability* (Courier Corporation, 2009).

Acknowledgments

Funding: This work was supported by Research Grants Council (RGC) (project nos. 17200320, 17200722, 17201523, and C6004-22Y) and Environment and Conservation Fund (project no. 125/2021). This work was also supported by the Health@InnoHK program of the Innovation and Technology Commission of the Hong Kong SAR Government. **Author contributions:** Conceptualization: L.X. and H.L. Methodology: L.X., H.L., W.Z., and X.L. Investigation: H.L. and W.Z. Visualization: H.L. and W.Z. Supervision: L.X. and X.L. Writing—original draft: L.X., H.L., and W.Z. Writing—review and editing: L.X., H.L., W.Z., and X.L. **Competing interests:** The authors declare that they have no competing interests. **Data and materials availability:** All data needed to evaluate the conclusions in the paper are present in the paper and/or the Supplementary Materials.

Submitted 5 February 2024
Accepted 21 May 2024
Published 26 June 2024
10.1126/sciadv.ado1019